SOLAR CELLS

Electron-hole diffusion lengths > 175 μm in solution-grown $CH_3NH_3PbI_3$ single crystals

Qingfeng Dong,[1]* Yanjun Fang,[1]* Yuchuan Shao,[1]* Padhraic Mulligan,[2] Jie Qiu,[2] Lei Cao,[2] Jinsong Huang[1]†

Long, balanced electron and hole diffusion lengths greater than 100 nanometers in the polycrystalline organolead trihalide compound $CH_3NH_3PbI_3$ are critical for highly efficient perovskite solar cells. We found that the diffusion lengths in $CH_3NH_3PbI_3$ single crystals grown by a solution-growth method can exceed 175 micrometers under 1 sun (100 mW cm^{-2}) illumination and exceed 3 millimeters under weak light for both electrons and holes. The internal quantum efficiencies approach 100% in 3-millimeter-thick single-crystal perovskite solar cells under weak light. These long diffusion lengths result from greater carrier mobility, longer lifetime, and much smaller trap densities in the single crystals than in polycrystalline thin films. The long carrier diffusion lengths enabled the use of $CH_3NH_3PbI_3$ in radiation sensing and energy harvesting through the gammavoltaic effect, with an efficiency of 3.9% measured with an intense cesium-137 source.

Demonstrated optoelectronic applications of organolead trihalide perovskites include high-efficiency photovoltaic cells (*1*–*3*), lasers (*4*), light-emitting diodes (*5*), and high-gain photodetectors (*6*), but the understanding of their fundamental properties, such as carrier diffusion length, has lagged behind. The carrier diffusion length in $CH_3NH_3PbI_3$ (henceforth $MAPbI_3$) should be sensitive to defects. Point defects in $MAPbI_3$ do not constitute midgap trap states (*7*), but a large density of charge traps has been broadly observed at the grain boundaries and surfaces of $MAPbI_3$ polycrystalline (MPC) films (*8*, *9*). We showed that the carrier diffusion length of MPC films increased to 1 μm when solvent annealing was used to enlarge the grain size to the thickness of the film (*10*). Determining the limit of carrier diffusion length requires larger $MAPbI_3$ single crystals (MSCs). We grew millimeter-sized MSCs using a low-temperature solution approach and characterized their fundamental electronic properties. Both electrons and holes were found to have diffusion lengths of >175 μm under 1 sun illumination and >3 mm in MSCs under weak illumination (0.003% sun).

Large-sized MSC growth from a supersaturated $MAPbI_3$ solution used a top-seeded solution-growth (TSSG) method (fig. S1) with a temperature gradient. Small-sized MSCs at the bottom of the container maintained the MA^+, Pb^{2+}, and I^- ion concentration for a saturated solution; the cooler top half of the solution was supersaturated. The large MSCs were grown by the consumption of small MSCs in the bottom. The small temperature difference between the bottom and the top of the solution induced sufficient convection to transport the material to the large MSCs. The as-grown MSCs had an average size of 3.3 mm and a largest size of ~10 mm (Fig. 1A); powder x-ray diffraction (XRD) (Fig. 1B) confirmed the tetragonal structure. Single-crystal XRD was best fit with an *I*4/*m* space group, in agreement with the results of Baikie *et al.* (*11*). The goodness of fit was 1.154, and the crystal data are summarized in tables S1 and S2.

We fabricated MSC photovoltaic devices by depositing 25-nm gold (Au) layers on one crystal facet as anodes and contacting gallium (Ga) with the opposite facet as cathodes (Fig. 2A). Thin MSCs with a thickness of 100 to 200 μm were peeled off from the large MSCs to fabricate MSC devices with thicknesses of either >3 mm or 200 μm. The optical and electrical properties of MSCs were compared with those of the 600-nm-thick solvent-annealed MPC thin films formed by the interdiffusion method (*10*). The MSCs displayed an extended absorption band to 850 nm, whereas regular MPC thin films had an absorption cutoff at 800 nm (Fig. 2B), which is consistent with the external quantum efficiency (EQE) of devices made of these two types of materials (Fig. 2C). These MSC devices differed from other MPC thin-film devices in that they exhibited a strong exciton absorption at 790 nm that was more intense in the thicker devices. The red shift of the EQE cutoff by 50 nm to 850 nm in the MSCs increased the upper limit of short-circuit current density (J_{SC}) in $MAPbI_3$-based solar cells from 27.5 mA cm^{-2} to 33.0 mA cm^{-2}. The photoluminescence (PL) peak of the MSCs, 770 nm, had a shorter wavelength than the exciton peak (Fig. 2C), which indicates that all of the excitons generated in MSCs dissociate to free charges at room temperature; and the band gap of the MSCs should be 1.61 eV. The blue-shifted and narrower PL peak indicates a lower trap density in MSCs.

The EQE of a 3-mm-thick MSC solar cell (Fig. 2D) ranged from 12.6 to 15.8% for wavelengths from 520 to 810 nm. The EQE of the MSC device decreased for shorter wavelengths, which suggests that the Au-MSC interface contains a large defect density (shorter wavelengths generate carriers closer to the MSC surface). These defects are most likely from the Pb^{2+} clusters formed by partial loss of the more soluble methylammonium iodide (MAI) when the single crystal

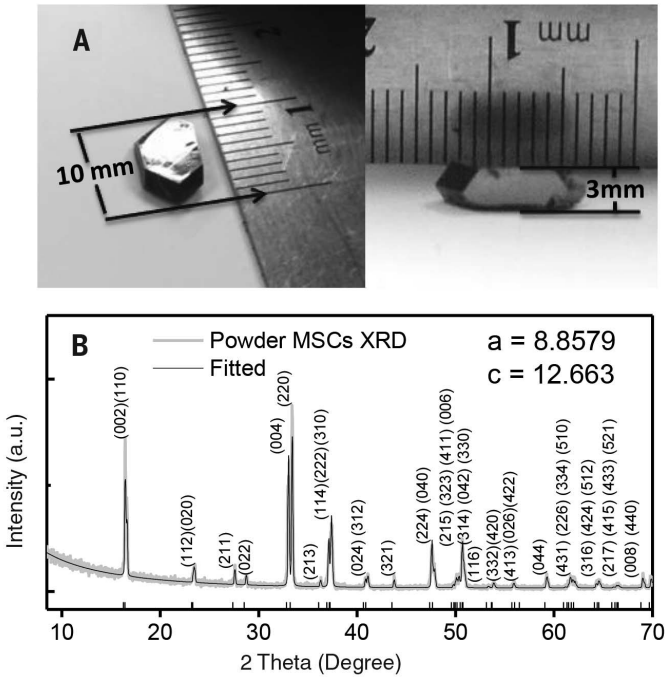

Fig. 1. MSC structure characterization. (**A**) Images of a piece of as-prepared $MAPbI_3$ single crystal. (**B**) X-ray diffraction pattern of the ground powder of a single crystal (gray line) and fitted patterns (black line).

[1]Department of Mechanical and Materials Engineering, University of Nebraska, Lincoln, NE 68588, USA. [2]Nuclear Engineering Program, Department of Mechanical and Aerospace Engineering, Ohio State University, Columbus, OH 43210, USA.
*These authors contributed equally to this work. †Corresponding author. E-mail: jhuang2@unl.edu

is removed from solution. Our recent density functional theory calculation verified that the Pb^{2+} clusters on the $MAPbI_3$ surface tend to form charge traps (*6*). The internal quantum efficiency (IQE) of the 3-mm MSC device (derived by dividing EQE by the transmittance of the Au electrode; see Fig. 2D and fig. S2) was near unity (95 ± 7%).

The electrons generated in the very thin perovskite layer near the Au anode must traverse the whole crystal to be collected by the Ga cathode, indicating that the electron diffusion length in MSCs is greater than the crystal thickness (~3 mm). We also replaced Ga by a semitransparent Au (25 nm)/C_{60} (25 nm) layer as the cathode so that photogenerated charges would be located at the cathode side. Again, the value of J_{SC} measured at 0.1% sun was comparable with incident light from both sides, which indicates that the hole diffusion length in MSCs is also longer than the MSC thickness.

The dependence of responsivity (R) and J_{SC} on light intensity (I_L) for thick devices is summarized in Fig. 2, E and F, respectively [see fig. S3 for photocurrent density–voltage (J_{ph}-V) curves]. Under 1 sun, the open-circuit voltage V_{oc} was 0.62 V, versus ~1.00 V in optimized MPC thin-film devices, again indicating a strong charge recombination in the MSC devices under strong illumination. For thick MSC devices, R decreased from 35 mA W^{-1} to 0.19 mA W^{-1} when the intensity of white illuminated light increased from 0.003 mW cm^{-2} to 100 mW cm^{-2} because of increased charge recombination for higher I_L. Fitting of J_{sc} with I_L as $J_{sc} \propto I_L^{\beta}$ gave a value of β (recombination parameter) of 0.5 ± 0.01, which suggests that second-order charge recombination dominated in the thick MSC devices for $I_L >$ 0.003 mW cm^{-2}, as seen previously (*12*, *13*). Reducing the MSC thickness to 200 μm recovered large R (Fig. 2E) at 1 sun and increased β to 0.88, which indicates that the carrier diffusion length of MSCs is near 200 μm for 1 sun illumination.

We could characterize the carrier mobility μ and carrier lifetime τ_r because the carrier diffusion length L_D is determined by $L_D = (k_B T \mu \tau_r / e)^{1/2}$, where k_B, T, and e are the Boltzmann constant, absolute temperature, and elementary charge, respectively. The device dark current (J_D) was measured to derive the trap density and carrier mobilities. The MSCs were sandwiched by two Au electrodes deposited by thermal evaporation to form hole-only devices. As shown in Fig. 3A, the linear J_D-V relation (green line) indicates an ohmic response at the low bias (< 2.1 V). A trap-filling process was identified by the marked increase of the current injection at a bias range of 2.1 to 10.7 V. The voltage at which all the traps are filled (trap-filled limit voltage V_{TFL}) was determined by the trap density (*14*):

$$V_{TFL} = \frac{e n_t L^2}{2\varepsilon\varepsilon_0} \quad (1)$$

where L is the thickness of the MSCs, ε (= 32) is relative dielectric constant of $MAPbI_3$, and ε_0 is the vacuum permittivity. The trap density n_t in MSCs was calculated to be 3.6 × 10^{10} cm^{-3}. For comparison, the hole-only devices with MPC thin films were also fabricated with PEDOT:PSS and Au as the hole injection electrodes (fig. S4). The calculated hole trap density in the MPC thin films was 2.0 × 10^{15} cm^{-3}, which is almost five orders of magnitude greater than in the MSCs. Thermal admittance spectroscopy (fig. S5) confirmed the reduction in trap density by two to three orders of magnitude in MSCs. Thus, the extraordinary carrier diffusion length in the MSCs is the result of largely suppressed trap density. When operating in the trap-free space charge limit current (SCLC) regime above 10.7 V, the dark current of the MSC was well fitted (Fig. 3A, green line) by the Mott-Gurney law:

$$J_D = \frac{9\varepsilon\varepsilon_0 \mu V_b^2}{8L^3} \quad (2)$$

where V_b is applied voltage. A large hole mobility of 164 ± 25 cm^2 V^{-1} s^{-1} was derived from the curve fitting. The uncertainties we reported represent a single standard deviation in the measurements on 10 nominally identical devices. Hall effect measurements revealed that the MSC was slightly p-doped, with a low free hole concentration of 9 (±2) × 10^9 cm^{-3} (see supplementary materials). The hole mobility from Hall effect measurement was 105 ± 35 cm^2 V^{-1} s^{-1}, in agreement with the SCLC results. Similarly, the electron trap density and electron mobility of MSCs were measured with the electron-only devices, which had phenyl-C_{61}-butyric acid methyl (PCBM):C_{60}/Ga as both electrodes. A low electron trap density of 4.5 × 10^{10} cm^{-3} was derived (Fig. 3B), comparable to the hole trap density, and the electron mobility was 24.8 ± 4.1 cm^2 V^{-1} s^{-1}. Finally, we used time-of-flight (ToF) to verify the high electron mobilities of 24.0 ± 6.8 cm^2 V^{-1} s^{-1} (Fig. 3, C and D). The electron and hole mobilities in MSCs are several times the intrinsic band transport mobility in MPC thin films (*10*) and polycrystals (*15*) measured by the Hall effect method

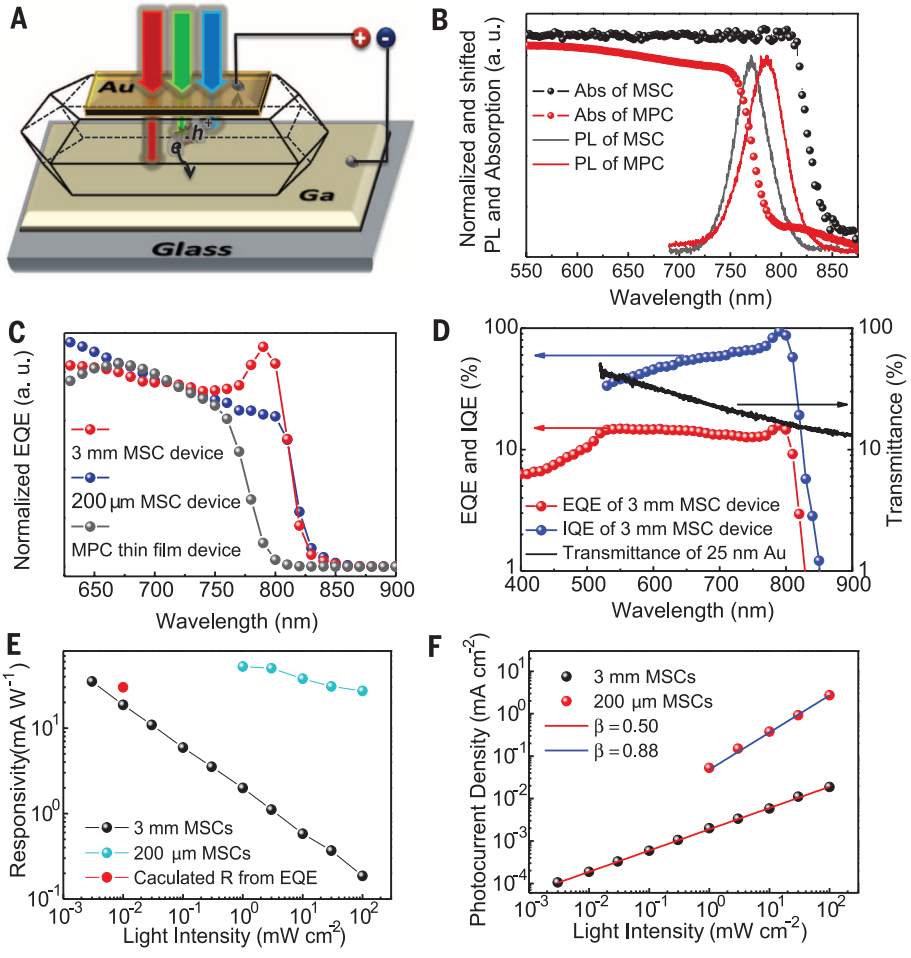

Fig. 2. Device structure and electrical and optical characterization of the MSC devices and MPC thin films. (**A**) Schematic device structure of the $MAPbI_3$ single-crystal devices. (**B**) Normalized PL and absorption spectra of the MSCs and MPC thin films. (**C**) Normalized EQEs of 3-mm-thick and 200-μm-thick MSC photovoltaic devices and a MPC thin-film device. (**D**) EQE of a 3-mm-thick MSC device, average transmittance of a 25-nm Au electrode, and calculated average IQE of the same MSC device. (**E**) Responsivity of the 3-mm-thick and 200-μm-thick MSC devices and responsivity calculated from the EQE of the 3-mm-thick MSC device. (**F**) Current density J_{sc} versus light intensity I_L fitted by $J_{SC} \propto I_L^{\beta}$ for the 3-mm-thick and 200-μm-thick MSC devices.

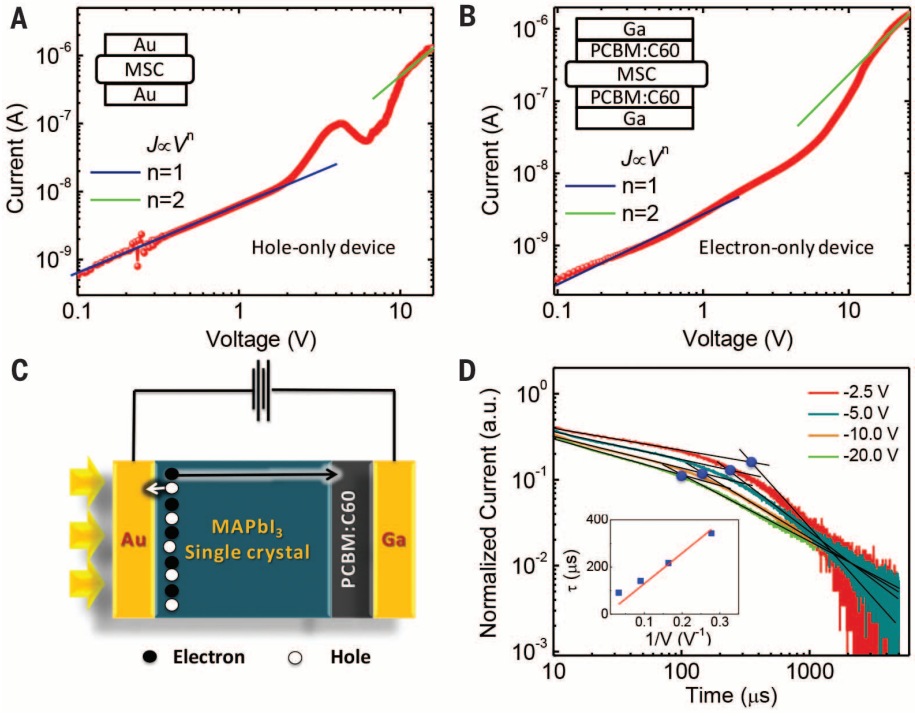

Fig. 3. Carrier mobility characterization of MSCs. (**A** and **B**) Current-voltage curve for a hole-only MSC device (A) and an electron-only MSC device (B). The insets show the device structure of hole-only and electron-only MSC devices, respectively. Three regions can be identified according to different values of the exponent *n*: *n* = 1 is the ohmic region, *n* = 2 is the SCLC region, and in between is the trap-filled limited region. (**C**) Schematic illustration of the device for the time-of-flight measurement. (**D**) The transient current curves of the MSC device show the normalized transient photocurrent under various reverse biases. The carrier transit time is determined by the intercept of the pretransit and posttransit asymptotes of the photocurrent, marked by solid blue circles. Inset shows the charge transit time versus the reciprocal of bias; the solid line is a linear fit to the data.

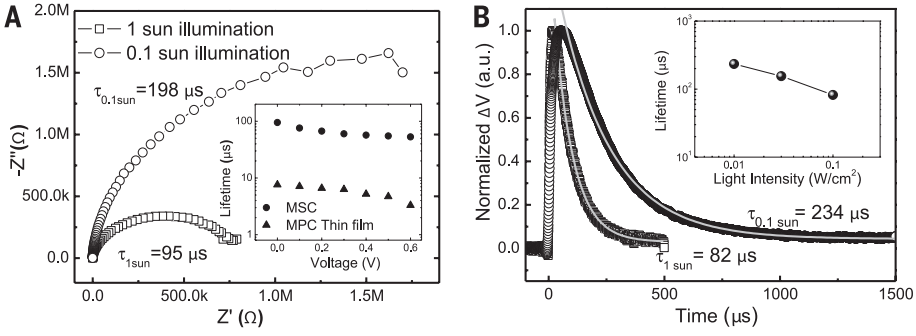

Fig. 4. Carrier recombination lifetime characterization of MSCs. (**A** and **B**) Impedance spectroscopies (A) and transient photovoltaic curves (B) of the MSC devices under 1 sun and 0.1 sun illumination, respectively, with incident light from the semitransparent Au anode. The TPV decay curves were fitted by a single-exponential decay function. The inset of (A) is the extracted charge recombination lifetime from IS measurement of the MSC device and the MPC thin film at various applied voltage biases under 1 sun illumination. The inset of (B) is the extracted charge recombination lifetime from TPV measurement of the MSC device under various light bias intensities.

and those measured by transient terahertz spectroscopy (*16*), both of which measure band transport mobility. However, ToF and SCLC mobilities are sensitive to the presence of charge traps in the materials. The excellent agreement of Hall mobility with ToF and SCLC mobilities in the single-crystal $MAPbI_3$ devices indicates that the band-tail states in the organolead trihalide perovskite single crystals are negligible.

We measured τ_r in MSCs with transient photovoltaic (TPV) and impedance spectroscopy (IS) at different values of I_L (Fig. 4); at 1 sun, the TPV and IS values of τ_r were 82 ± 5 μs and 95 ± 8 μs, respectively, more than 10 times the τ_r values in the best thin-film devices with sophisticated surface passivation (*10*). Combining the measured mobility and lifetime of MSCs, the hole diffusion length is 175 ± 25 μm under 1 sun. The measured bulk carrier lifetime can be underestimated because of the presence of surface charge recombination, so the bulk carrier diffusion length should exceed this value. Reducing the bias light intensity to 0.1 sun increased τ_r to 234 and 198 μs by TPV and IS measurements, respectively, indicating a longer carrier diffusion length under weaker light intensity.

The long carrier diffusion length of $MAPbI_3$ can find direct application in x-ray and gamma-ray sensing and in radiation energy harvesting. Radiation is generally much weaker than 1 sun but should penetrate the entire device. Details pertaining to the carrier diffusion length extrapolation under weak light, radiation measurement, simulation, and estimation of gammavoltaic efficiency can be found in the supplementary materials. We extrapolated a carrier recombination lifetime of 2.6 ± 0.2 s and carrier diffusion length sum of 33 ± 5 mm under a light intensity of 0.003 mW cm^{-2} from our 1 sun data. The presence of surface recombination should reduce the carrier diffusion length, and the measured >3 mm electron and hole diffusion length under weak light is thus reasonable. We exposed the 3-mm MSC device to intense gamma radiation and measured the electric current generation. A cesium-137 gamma irradiator of 102 Ci yielded a persistent current of 36.3 ± 0.3 nA, which corresponds to a photon-to-electron conversion efficiency of 3.9% and agrees with the theoretic estimation.

The demonstrated high carrier mobility, carrier lifetime, and diffusion length of the MSCs described above point to several new directions for the application of $MAPbI_3$ materials in printable electronics, lasers, and solar cells (*4*). The high PL quantum yield of $MAPbI_3$ and the excellent overlap of the PL spectra with the absorption spectrum of the single crystal allow photon recycling in thick perovskite crystals by reabsorbing the emission (*4*, *5*). The demonstration of a charge diffusion length that greatly exceeds the absorption depth of photons with energy larger than the band gap of perovskites implies that IQEs of essentially 100% can be achieved under the low internal electric fields at device working condition.

REFERENCES AND NOTES

1. S. D. Stranks *et al.*, *Science* **342**, 341–344 (2013).
2. M. M. Lee, J. Teuscher, T. Miyasaka, T. N. Murakami, H. J. Snaith, *Science* **338**, 643–647 (2012).
3. A. Mei *et al.*, *Science* **345**, 295–298 (2014).
4. G. Xing *et al.*, *Nat. Mater.* **13**, 476–480 (2014).
5. Z. K. Tan *et al.*, *Nat. Nanotechnol.* **9**, 687–692 (2014).
6. R. Dong *et al.*, *Adv. Mater.* 10.1002/adma.201405116 (2015).
7. J. Kim, S. H. Lee, J. H. Lee, K. H. Hong, *J. Phys. Chem. Lett.* **5**, 1312–1317 (2014).
8. N. K. Noel *et al.*, *ACS Nano* **8**, 9815–9821 (2014).
9. I. A. Shkrob, T. W. Marin, *J. Phys. Chem. Lett.* **5**, 1066–1071 (2014).
10. Z. Xiao *et al.*, *Adv. Mater.* **26**, 6503–6509 (2014).
11. T. Baikie *et al.*, *J. Mater. Chem. A* **1**, 5628–5641 (2013).
12. J. S. Manser, P. V. Kamat, *Nat. Photonics* **8**, 737–743 (2014).
13. S. D. Stranks *et al.*, *Phys. Rev. A* **2**, 034007 (2014).
14. R. H. Bube, *J. Appl. Phys.* **33**, 1733–1737 (1962).
15. C. C. Stoumpos, C. D. Malliakas, M. G. Kanatzidis, *Inorg. Chem.* **52**, 9019–9038 (2013).
16. C. Wehrenfennig, G. E. Eperon, M. B. Johnston, H. J. Snaith, L. M. Herz, *Adv. Mater.* **26**, 1584–1589 (2014).

ACKNOWLEDGMENTS

Supported by U.S. Department of Energy award DE-EE0006709 (solar cell) and Defense Threat Reduction Agency award HDTRA1-14-1-0030 (radiation detector). J.H. conceived the idea and supervised the project; Q.D. grew the single crystals and fabricated the devices; Q.D., Y.F., and Y.S. conducted the electric and optical characterization of the devices; P.M., J.Q., and L.C. measured the devices under gamma ray irradiation and did the simulation; and J.H. wrote the paper.

SUPPLEMENTARY MATERIALS

www.sciencemag.org/content/347/6225/967/suppl/DC1
Materials and Methods
Figs. S1 to S11
Tables S1 and S2
References (*17*–*21*)

27 December 2014; accepted 20 January 2015
Published online 29 January 2015;
10.1126/science.aaa5760

WATER SPLITTING

Metal-free efficient photocatalyst for stable visible water splitting via a two-electron pathway

Juan Liu,[1] Yang Liu,[1] Naiyun Liu,[1] Yuzhi Han,[1] Xing Zhang,[1] Hui Huang,[1] Yeshayahu Lifshitz,[1,2]* Shuit-Tong Lee,[1]* Jun Zhong,[1] Zhenhui Kang[1]*

The use of solar energy to produce molecular hydrogen and oxygen (H_2 and O_2) from overall water splitting is a promising means of renewable energy storage. In the past 40 years, various inorganic and organic systems have been developed as photocatalysts for water splitting driven by visible light. These photocatalysts, however, still suffer from low quantum efficiency and/or poor stability. We report the design and fabrication of a metal-free carbon nanodot–carbon nitride (C_3N_4) nanocomposite and demonstrate its impressive performance for photocatalytic solar water splitting. We measured quantum efficiencies of 16% for wavelength λ = 420 ± 20 nanometers, 6.29% for λ = 580 ± 15 nanometers, and 4.42% for λ = 600 ± 10 nanometers, and determined an overall solar energy conversion efficiency of 2.0%. The catalyst comprises low-cost, Earth-abundant, environmentally friendly materials and shows excellent stability.

Production of hydrogen and oxygen from water is a promising means of storing solar energy in a way that compensates for the intermittency of sunlight as a primary source of power (*1*, *2*). It can be realized by applying a hybrid system in which a solar cell powers an electrolyzer [photovoltaic (PV) electrolysis]. Photoelectrolysis (PE) uses photocatalyst electrodes with additional electrical power provided by a photovoltaic element. Photocatalysis (PC) involves light-irradiated catalysts (typically catalyst powders suspended in water) for water splitting (*3*). Recently reported "solar-to-hydrogen" (STH) efficiencies for PV electrolysis systems exceed 10% (*4*–*6*). State-of-the-art PE systems yield STH values of 2 to 3% (*7*) but are believed to provide a cheaper solution for H_2 production. PC is the simplest water-splitting approach, more amenable to cheap, large-scale applications of H_2 generation. Unfortunately, despite intense efforts during the past 40 years (*8*–*15*), current direct photocatalysts for water splitting still face several challenging issues: (i) Currently reported catalysts suffer from low quantum efficiency (QE) in the visible range, with STH efficiencies less than 0.1% (*16*–*18*); (ii) many photocatalysts are made of rare and expensive materials; (iii) various photocatalysts show poor stability [e.g., inorganic sulfide and (oxy)nitride-based photocatalysts are less stable and more susceptible to oxidation than water]; (iv) O_2 release from semiconductor catalysts is difficult, so that the use of sacrificial reagents is required; (v) the overall four-electron water oxidation to O_2 encounters a large overpotential; and (vi) the kinetically competing two-electron reaction to H_2O_2 often poisons the photocatalysts (*19*).

Overall water splitting to H_2 and O_2 requires a high free energy of 113.38 kcal/mol (*20*, *21*). The challenge lies mainly in the release of diatomic O_2, which involves four electron and four proton transfers for the eventual formation of an O-O bond. The concerted four-electron process for oxygen evolution (1.23 eV) is thermodynamically more favorable than the two-electron process for H_2O_2 formation (1.78 eV). However, detailed analysis (see supplementary text) shows that a higher reaction rate may be achieved in a system where water is first oxidized via a two-electron reaction to H_2O_2 and H_2, followed by H_2O_2 decomposition to O_2 and H_2O. For this stepwise two-electron/two-electron water splitting to H_2 and O_2 to be viable and practical, the photocatalyst applied should be capable of promoting generation as well as subsequent decomposition of H_2O_2 with high efficiencies and low overpotentials, so as to allow considerable reduction in the energy cost for production of H_2 and O_2 via overall water splitting. Here, we report that nanocomposites of carbon nanodots embedded in a C_3N_4 matrix perform as an excellent photocatalyst fulfilling the above requirements.

C_3N_4 is commercially available (e.g., from Carbodeon) and can be easily fabricated (e.g., from urea) (*19*). It is an Earth-abundant and low-cost photocatalyst capable of generating H_2 and H_2O_2 from water even in the absence of catalytic metals, albeit with a low QE (*19*, *22*–*26*). C_3N_4 belongs to the oldest reported polymer materials prepared by chemists (by Berzelius in ~1830) and first termed "Melon" (*27*). In 2006 it was determined that the visible light activity of TiO_2 after treatment with urea was due to "Melon" (*28*). In 2009, Antonietti and colleagues described in detail the optical properties, electronic structure, and photocatalytic activity of C_3N_4 (*29*). Following this work, many groups attempted to optimize the catalytic properties of C_3N_4, motivated by its relatively low band gap energy E_g of 2.7 eV, and high valence band and conduction band positions (*29*) [1.8 and −0.9 eV versus reversible hydrogen electrode (RHE)]. Many heterojunction composites with oxide semiconductors as well as photocatalyst systems were investigated. The latter included systems with a variety of oxides (*30*) and sulfides (*31*) along with pure metals (*19*) and even graphene (*32*) and carbon nanotubes (*33*). Different preparation methods were studied in an effort to increase the surface area of C_3N_4 and to improve its catalytic activity. The QE values obtained using C_3N_4 as a catalyst for water splitting to H_2 and O_2 have been low (maximum 3.75% at 420 nm and less than 0.5% for 500 nm), and generally the use of a sacrificial reagent has been necessary (*19*, *24*, *26*, *30*–*32*, *34*). The efficiency at 700 nm can be largely increased by applying dye molecules, but again a sacrificial reagent is a must (*35*). During water splitting C_3N_4 suffers from poisoning by the produced H_2O_2, which is difficult to remove from the C_3N_4 surface (*19*). Different methods including stirring, bubbling, and/or addition of chemical agents have been attempted for regeneration of the poisoned C_3N_4 catalyst (*19*).

Carbon nanodots (CDots; monodisperse graphite particles less than 10 nm in diameter) exhibit unique photo-induced electron transfer, photoluminescence, and electron reservoir properties (*36*). In particular, CDots possess high catalytic activity (by chemical catalysis; no light is needed) for H_2O_2 decomposition (*37*). Given the photocatalytic properties of CDots and C_3N_4, we hypothesized that a combination of CDots and C_3N_4 could constitute a high-performance composite photocatalyst for water splitting via the stepwise two-electron/two-electron process: (i) $2H_2O \rightarrow H_2O_2 + H_2$; (ii) $2H_2O_2 \rightarrow 2H_2O + O_2$.

[1]Jiangsu Key Laboratory for Carbon-based Functional Materials and Devices, Institute of Functional Nano and Soft Materials (FUNSOM), Soochow University, Suzhou 215123, China. [2]Department of Materials Science and Engineering, Technion, Israel Institute of Technology, Haifa 3200003, Israel.
*Corresponding authors. E-mail: zhkang@suda.edu.cn (Z.K.); apannale@suda.edu.cn (S.-T.L.); shayli@tx.technion.ac.il (Y.L.)

Electron-hole diffusion lengths > 175 μm in solution-grown $CH_3NH_3PbI_3$ single crystals

Qingfeng Dong *et al.*

Science **347**, 967 (2015);
DOI: 10.1126/science.aaa5760

Science (print ISSN 0036-8075; online ISSN 1095-9203) is published weekly, except the last week in December, by the American Association for the Advancement of Science, 1200 New York Avenue NW, Washington, DC 20005.